drones

MDPI

Article

Novel Design and Computational Fluid Dynamic Analysis of a Foldable Hybrid Aerial Underwater Vehicle

Guangrong Chen [1,2,*,†], Lei Yan [2,†], Ao Cao [2], Xinyuan Zhu [2], Hongbo Ding [2] and Yuxiang Lin [3]

[1] Tangshan Research Institute, Beijing Jiaotong University, Tangshan 063000, China
[2] Robotics Research Center, Beijing Jiaotong University, Beijing 100044, China; 22126068@bjtu.edu.cn (L.Y.); 23126066@bjtu.edu.cn (A.C.); 23121282@bjtu.edu.cn (X.Z.); 23126058@bjtu.edu.cn (H.D.)
[3] Dundee International Institute, Central South University, Changsha 410004, China; 2542715@dundee.ac.uk
* Correspondence: grchen@bjtu.edu.cn
† These authors contributed equally to this work.

Abstract: Hybrid Aerial Underwater Vehicles (HAUVs), capable of operating effectively in both aerial and underwater environments, offer promising solutions for a wide range of applications. This paper presents the design and development of a novel foldable wing HAUV, detailing the overall structural framework and key design considerations. We employed fluid simulation software to perform comprehensive hydrodynamic and aerodynamic analyses, simulating the vehicle's behavior during aerial flight, underwater navigation, water entry and exit, and surface gliding. The motion characteristics under different speed and angle conditions were analyzed. Additionally, a physical prototype was constructed, and experimental tests were conducted to evaluate its performance in both aerial and underwater environments. The experimental results confirmed the vehicle's ability to seamlessly transition between air and water, demonstrating its viability for dual-environment operations.

Keywords: hybrid aerial underwater vehicle; foldable wings; computational fluid dynamic; multimodal

Citation: Chen, G.; Yan, L.; Cao, A.; Zhu, X.; Ding, H.; Lin, Y. Novel Design and Computational Fluid Dynamic Analysis of a Foldable Hybrid Aerial Underwater Vehicle. *Drones* **2024**, *8*, 669. https://doi.org/10.3390/drones8110669

Academic Editor: Abdessattar Abdelkefi

Received: 20 September 2024
Revised: 8 November 2024
Accepted: 11 November 2024
Published: 12 November 2024

1. Introduction

The exploration of the ocean and atmosphere is critical for scientific research, environmental monitoring, and defense applications. Hybrid Aerial Underwater Vehicles (HAUVs), which can seamlessly transition between aerial and underwater environments, have emerged as key technologies to meet these needs [1,2]. Their versatility enables them to traverse both air and water, facilitating continuous, large-scale environmental monitoring and enhancing operational capabilities across a wide range of applications, including underwater exploration, surveillance, and resource management [3,4]. As the demand for multi-environment exploration grows, the development of advanced HAUVs has become increasingly important [5,6].

In recent years, significant advancements have been made in HAUV design and control strategies. Researchers have focused on improving the vehicles' ability to transition smoothly between air and water, enhancing their operational stability and performance in both environments. For example, Bi et al. introduced a novel miniaturized and lightweight HAUV, named "Nezha-mini", which weighs 953 g and is A4-sized. Its low cost and high modularity facilitate convenient repair and remanufacturing [7]. Additionally, they presented the design, construction, control, and oceanic testing of Nezha-IV, demonstrating reliability and robustness, particularly during transition phases [8]. They also developed a dynamic model and control strategies for a quadcopter-like HAUV to enable cross-domain locomotion under ocean disturbances [9]. Lu et al. presented an improved design for a multimodal HAUV capable of level and vertical flight, hovering, and underwater gliding [10,11]. They also introduced a nonlinear dynamic controller, known as the adaptive dynamic surface control (ADSC) scheme, which effectively addresses challenges arising from the system's nonlinearities, uncertainties, and time-varying parameters [12]. Aoki

et al. analyzed a hybrid unmanned aerial underwater vehicle considering environmental transitions [13]. Ravell et al. introduced a model for a multi-medium unmanned vehicle capable of seamless operation in air or underwater. This multi-medium system is treated as a hybrid system with continuous dynamics in both environments and discrete transitions during changes in medium density [14]. Horn et al. presented the HyDrone, a novel concept for hybrid vehicles in aerial and underwater applications. They introduced translation and rotation models in SE(3), along with control laws to stabilize the system in both environments [15]. Pinheiro et al. proposed a trajectory planning approach that allows for collision avoidance against unknown obstacles and smooth transitions between aerial and aquatic media [7]. Grando et al. utilized Deep Reinforcement Learning to achieve autonomous mapless navigation for Hybrid Unmanned Aerial Underwater Vehicles, which can operate in both air and water [16]. Ba et al. proposed a virtual-constraints-based end-effector pose compensator to guarantee high pose precision, and it can be employed on the pose control of HAUV [17]. From a biomimetic perspective [18], Zimmerman et al. investigated the buckling and dynamics of diving-inspired drones when entering water [19] and during diving [20,21]. Pena et al. studied the comprehensive sizing process, actuation mechanism selection, and development of gannet-inspired amphibious drones [22], and analyzed the performance and design process [23]. Wang et al. developed and fabricate an novel aerial-aquatic water-jet thruster, which uses butane and oxygen to realize explosive water-jet. An unit butane cell and oxygen cell can satisfy more than 50 explosions without replacement of components [24,25]. Gan et al. performed an aerodynamic/hydrodynamic investigation of water cross-over for a bionic unmanned aquatic–aerial amphibious vehicle [26].

In the field of HAUVs, foldable wings have gained particular attention due to their ability to optimize aerodynamic performance during flight and reduce drag during underwater navigation. Recent studies by Chen et al. [27,28] have explored the dynamic behavior of HAUVs with foldable wings, enhancing their control systems to ensure smooth transitions between air and water. These designs allow vehicles to adapt their wing configurations based on the environment, thereby enhancing maneuverability, minimizing energy consumption, and improving mission flexibility. Sun et al. presented the design and field tests of a foldable wing unmanned aerial–underwater vehicle (UAUV) [7]. Chen et al. also introduced a foldable hybrid aerial underwater vehicle that combines the structural characteristics of torpedoes and loitering munitions [29].

Despite these advancements, current HAUVs still face several challenges. Issues such as stability during medium transitions, energy efficiency, and performance optimization across various environments remain active research areas. While promising, foldable-wing mechanisms require further refinement to ensure robust performance in harsh underwater conditions. Additionally, control systems must adapt to the rapidly changing dynamics across different mediums. Furthermore, most existing designs focus on specific tasks, lacking the flexibility to handle a variety of operational scenarios. This research aims to address these challenges by introducing an advanced foldable-wing structure design coupled with an intelligent control system for improved adaptability and efficiency.

This paper introduces a novel foldable HAUV design optimized for performance in both air and water. It builds on existing designs while addressing key limitations related to aerodynamic and hydrodynamic efficiency. Unlike previous models that struggle with power efficiency and stability during transition phases, the proposed design integrates a robust folding wing mechanism that enhances both flight stability and underwater maneuverability.

Previous studies on HAUVs have primarily focused on static designs or limited folding mechanisms. In contrast, our design leverages advanced computational fluid dynamics (CFD) simulations to analyze aerodynamic and hydrodynamic interactions, offering a more detailed understanding of the vehicle's behavior in hybrid environments. This model provides greater adaptability and efficiency compared to simpler prototypes.

The main contributions of this paper are threefold:

- A novel foldable wing mechanism tailored for multi-environment adaptability.

- Comprehensive CFD simulations that provide detailed insights into aerodynamic and hydrodynamic performance.
- A performance evaluation framework that highlights energy efficiency, thrust-to-weight ratio, and transition capabilities in both air and water environments.

These contributions aim to address the gaps in current HAUV research, providing a more comprehensive solution for multi-environment missions. The novel structure of the vehicle is illustrated in Figure 1.

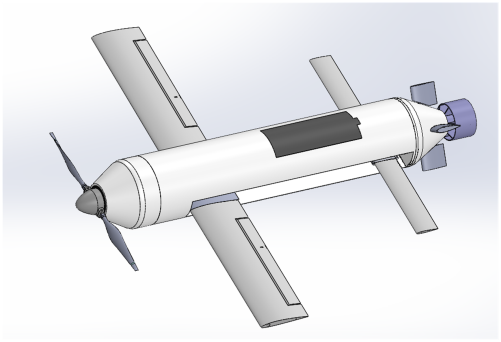

Vehicle wings deployed (aerial flight) state

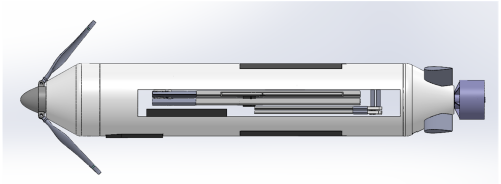

Vehicle wings folded (underwater submerged) state

Figure 1. Total schematic diagram of hybrid aerial underwater vehicle.

The remainder of this paper is organized as follows: Section 2 presents the design of the foldable HAUV. Section 3 introduces the computational fluid dynamics analysis of the designed HAUV. Section 4 describes the experimental setup and results. Finally, Section 5 concludes the paper and outlines potential future research directions.

2. Design

2.1. The Overall Configuration

To enable the vehicle to achieve high-speed flight in the air and high-speed navigation underwater while minimizing impact loads upon entering water and reducing resistance upon exiting, the foldable-wing aerial underwater vehicle combines the functionalities of fixed-wing unmanned aerial vehicles and underwater submersibles. This integration facilitates swift cruising, agile maneuvers, enduring operations, and covert advancements, allowing for seamless traversal through air and water to detect and engage aerial, terrestrial, surface, and underwater targets. The specific estimated performance metrics are detailed in Table 1.

Common aerodynamic layouts for fixed-wing unmanned vehicles include the conventional, delta-wing, tailless, canard, and flying wing layouts. To meet buoyancy requirements, wings are typically designed with extended wingspans and chord lengths. However, achieving miniaturization poses challenges, necessitating a wing-folding mechanism to stow the wings beneath the vehicle's fuselage and mitigate drag forces.

The overall structure of this foldable hybrid aerial underwater vehicle is shown in Figure 2. To meet the varying requirements of air flight and underwater navigation, the vehicle comprises a front foldable propeller mechanism, a body section, a foldable wings mechanism, a battery, an X-type rudder mechanism, and a tail submersible thruster mechanism.

Table 1. Performance parameters of the designed HAUV.

Parameter	Value
Air speed	80 km/h
Sneak speed	20 km/h
Forward wing span	600 mm
Rear wing span	360 mm
Body length	600 mm
Endurance	10 min
Maximum height	40 m
Maximum depth	3 m
Weight	2.5 kg

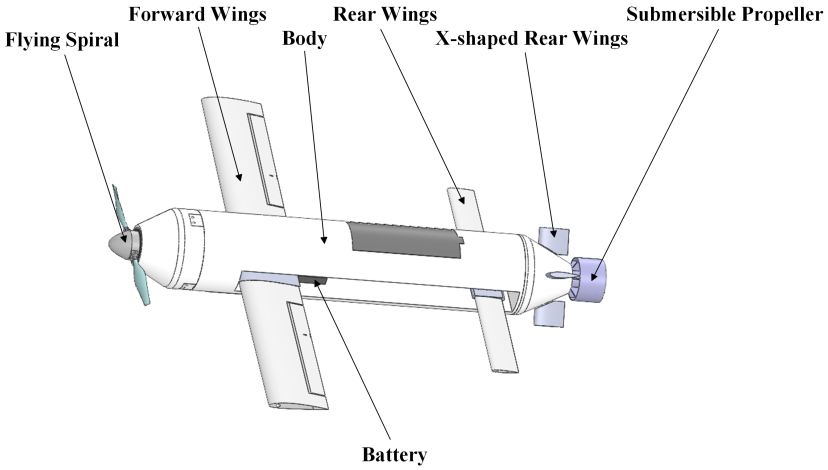

Figure 2. The overall configuration of hybrid aerial underwater vehicle.

This paper presents a comprehensive lightweight design of the hybrid aerial underwater vehicle, incorporating a sophisticated variable structure design and system layout tailored to diverse operational scenarios in both aerial and underwater environments. The vehicle encompasses three distinct motion states—airborne flight, surface gliding, and underwater navigation—along with two spanning states for entering and exiting the water. These configurations enable the vehicle to effectively execute designated tasks within different media (air and water). The vehicle's trajectory is illustrated in Figure 3. The overall control flow of the vehicle is shown in Figure 4. The trajectory diagram illustrates the motion dynamics as the vehicle transitions between air and water while executing various tasks. The control architecture of the vehicle ensures seamless navigation and effective task execution.

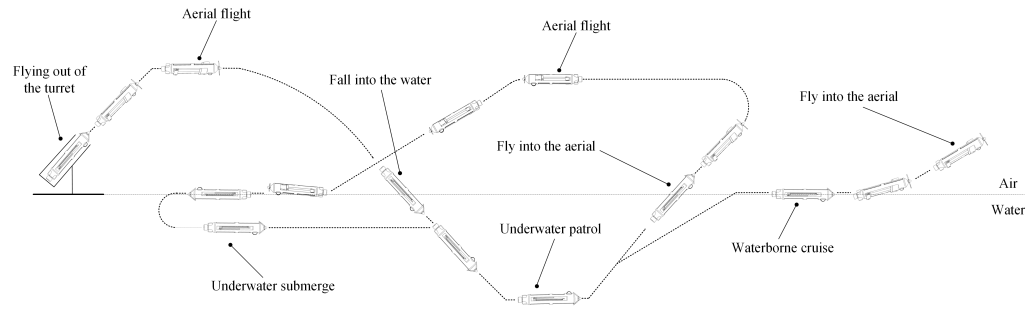

Figure 3. Operational flow chart of hybrid aerial underwater vehicle.

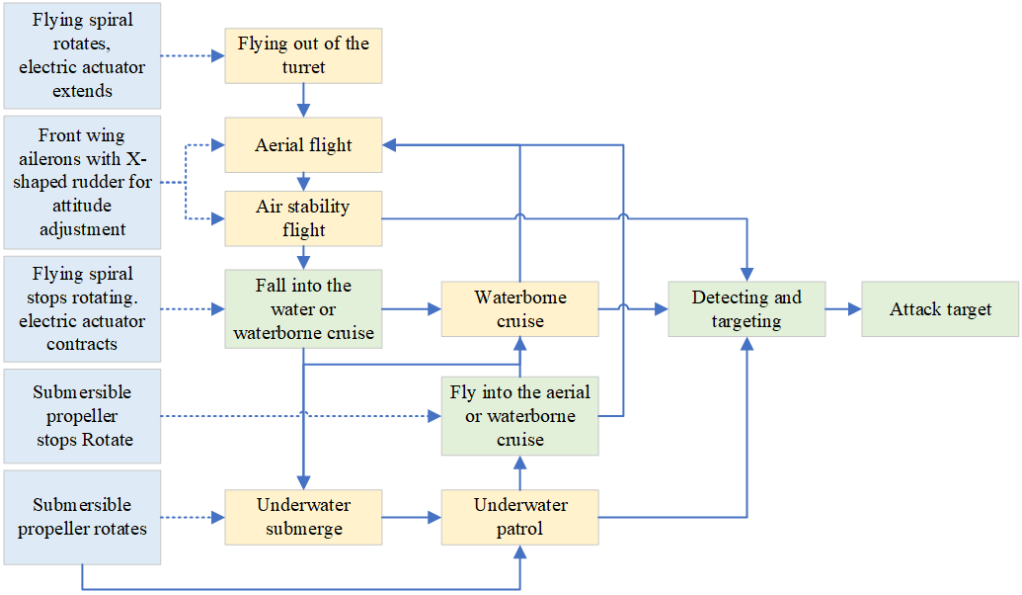

Figure 4. Control flow chart of hybrid aerial underwater vehicle.

2.2. Analysis of Wing Airfoil

In this paper, wing loading—the ratio of a vehicle's weight to its wing area—significantly impacts its range, takeoff, and landing performance. The calculation of wing loading involves stall speed, which is the speed at which the vehicle achieves equilibrium between lift and gravity during horizontal flight, operating at its maximum lift coefficient Chen et al. [30]. The calculation is performed using the following formula:

$$Mg = \frac{1}{2}\rho V_1^2 S C_L \tag{1}$$

where: M denotes the weight of the vehicle (kg); ρ denotes the air density (kg/m^3); S denotes the area of the wing of the vehicle (m^2); V_1 denotes the airborne stall speed (m/s); and C_L denotes the lift coefficient of the wing of the vehicle.

Given the sea-level air density ρ as 1.225 kg/m^3, the weight of the vehicle M as 2.5 kg, the maximum speed of the vehicle V_1 as 33 m/s, and the wing area of the vehicle S as 0.048 m^2, the calculated lift coefficient C_L amounts to 0.781. This relatively modest lift coefficient allows for a slight wing curvature, facilitating the maintenance of the launch direction at liftoff. This design is advantageous for preserving the vehicle's launch trajectory and stabilizing its motion attitude and direction post-launch.

Next, the Reynolds number during the vehicle's flight is calculated using the following equation:

$$Re = \frac{\rho V_2 L}{\mu} \tag{2}$$

In the context of the provided equations, the symbol Re signifies the Reynolds number; μ symbolizes the fluid viscosity in Pa·s units; V_2 represents the airborne cruise speed in meters per second; and L denotes the average aerodynamic chord length of the wing in meters.

Assuming the fluid viscosity μ is 1.8×10^{-5} Pa·s, the average aerodynamic chord length L of the wing is 0.08 m, the cruising speed V_2 is 22 m/s, and the Reynolds number is determined to be 119,778 through the aforementioned calculations. Ultimately, the Reynolds number Re is approximated to be 120,000.

This paper presents a cross-media vehicle designed to operate at moderate speeds in low-altitude shallow waters, drawing inspiration from small, low-speed aerial vehicles. The vehicle's wings are designed with four primary airfoil options: NACA0012, NACA0018, NACA2412, and NACA4412.

the four airfoils are imported into the xflr5 software for direct airfoil design, and the reynolds number re is selected as 120,000, resulting in the curves of lift, drag, pitching moment, and lift-to-drag ratio versus angle of approach for the four airfoils, as shown in the following Figures 5 and 6.

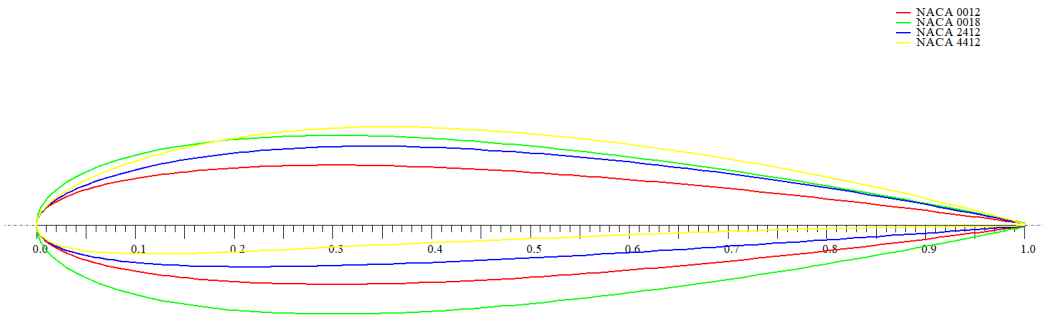

Figure 5. Four wing airfoils.

In Figure 6, the performance of these airfoils is compared. The NACA0012 airfoil exhibits the highest lift-to-drag ratio, peaking at a head-on angle of 5°. Both the NACA0018 and NACA2412 airfoils reach their maximum lift-to-drag ratios at around a head-on angle of 7°, with the NACA2412 demonstrating a superior ratio. In contrast, the NACA4412 achieves its peak lift-to-drag ratio at a head-on angle of 9°. Notably, the NACA2412 shows a higher lift-to-drag ratio and lift coefficient, along with a relatively smaller curvature compared to the NACA4412. Therefore, the NACA2412 airfoil is selected as the optimal front wing type.

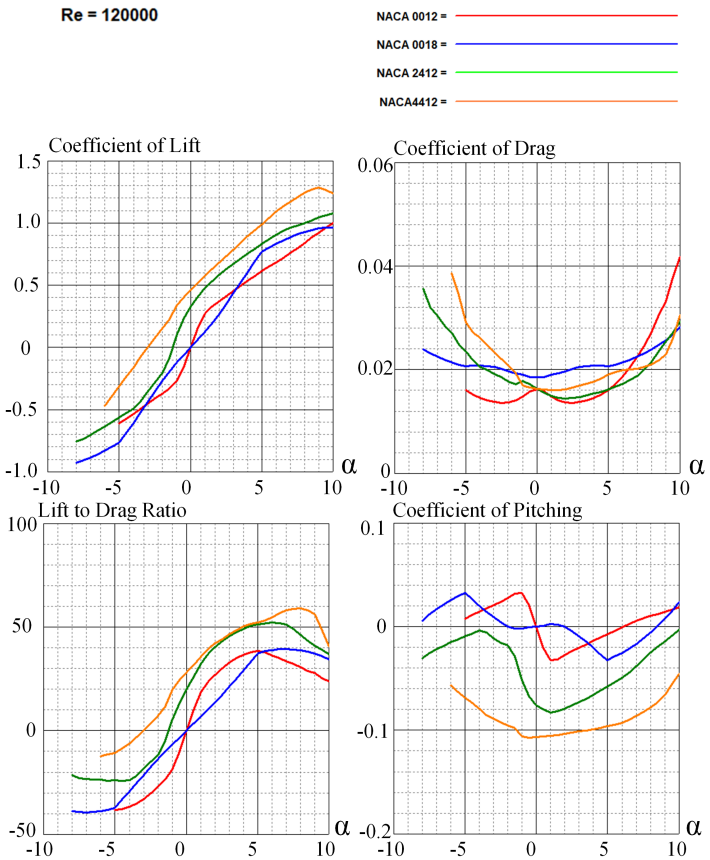

Figure 6. Curves of lift, drag, pitching moment and lift-to-drag ratio for four airfoil types with respect to angle of approach.

The primary function of the rear wings is to enhance vehicle stability, ensuring equilibrium during fluctuations in speed and altitude. Serving as a fixed horizontal stabilizing surface, the rear wing provides static pitch stability, helping to maintain the vehicle's orientation during ascent or descent. During horizontal flight, this surface does not exert additional moments on the vehicle. However, if the vehicle deviates from level flight, aerodynamic forces on the horizontal stabilizing surface generate moments that correct the pitch attitude, restoring it to horizontal flight. This mechanism stabilizes the vehicle regardless of whether it pitches up or down. Therefore, the rear wing must have a symmetrical design with minimal thickness to facilitate complete retraction into the fuselage. Thus, this study opts for the NACA0012 airfoil as the rear wing type.

The X-type rudder primarily governs the vehicle's pitch and yaw maneuvers, playing a crucial role in directional control. For consistent aerodynamic performance, the rudder's cross-section airfoil is aligned with the NACA0012 airfoil.

2.3. Design of Foldable Wings

The deployed configuration of the wing is illustrated in Figure 7. Initially, the electric actuator advances along the actuator slots, propelling the two front wing links forward. Both the front left and right wings then pivot simultaneously in opposite directions, completing a 90° rotation until secured by the fuselage. Subsequently, the electric pushrods move rearward, causing both rear wings to rotate 90° concurrently in the opposite direction. This sequence culminates in the front and rear wings reaching a fully extended position.

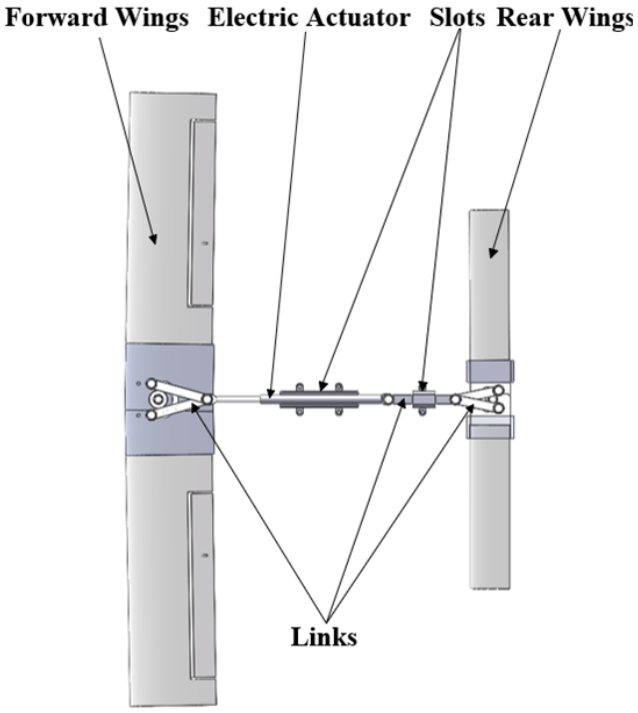

Figure 7. Deployed state diagram of foldable wing mechanism.

The folded configuration of the wing is depicted in Figure 8. Initially, the electric actuator progresses forward within the actuator slots, moving the two rear wing linkages. Both the rear left and right wings are then simultaneously rotated 90° in opposite directions until secured by the linkage slots. Finally, the electric actuator initiates backward movement, causing both front wings to rotate 90° simultaneously in opposite directions until the actuator reaches zero travel. This process results in both the front and rear wings being fully folded.

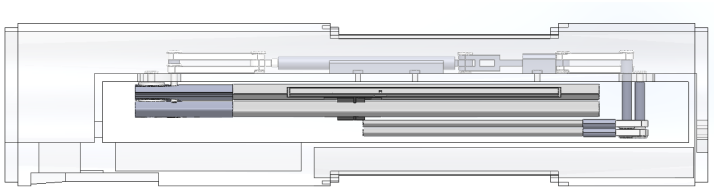

Figure 8. Folded state diagram of foldable wing mechanism.

2.4. Design of X-Type Rudder

As shown in Figure 9, the X-type rudder mechanism is installed in the fuselage at the rear of the streamlined slewing body shell, with the tail of the underwater thruster mechanism positioned forward. The two rudder fixing shafts are semi-circular and placed symmetrically in the same plane, forming a 90° X-type configuration. Each rudder fixing shaft is attached to the head and tail ends of each rudder, resulting in four rudders arranged symmetrically along the vertical and horizontal planes.

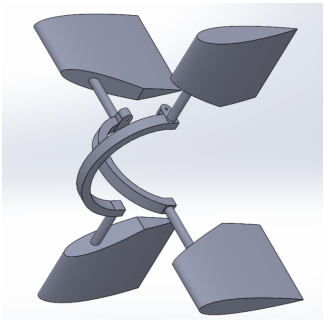

Figure 9. X-type Rudder mechanism.

3. Computational Fluid Dynamic Analysis

Computational Fluid Dynamics (CFD) utilizes computer technology to simulate the motion of complex fluids. Ansys Fluent software offers high solution accuracy and rapid convergence, effectively simulating the fluid flow process. The corresponding turbulence model can be selected according to varying flow conditions during the solution process. Therefore, based on the finite volume method, this paper establishes a high-precision numerical computational model of the HAUV using Ansys Fluent and analyzes various aspects of its aerodynamic and hydrodynamic performance.

3.1. Aerial Fluid Simulation and Analysis

Due to the complexity of the HAUV's 3D model, detailing the local mesh proves challenging. To address this, a smaller mesh size is employed to increase mesh quantity. However, this often results in unsuccessful mesh delineation or poor quality when directly inputting the original model into Fluent software Hou et al. [31]. To circumvent these issues, the original 3D model is streamlined before being introduced into the fluid simulation software. The simplified aerial model is shown in Figure 10.

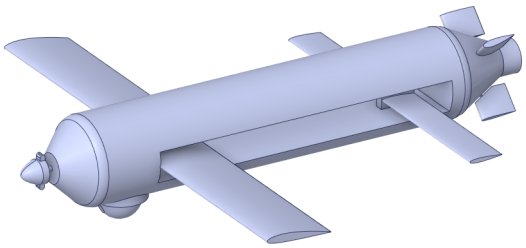

Figure 10. Simplified 3D model for the aerial flight state.

After importing the simplified model into Fluent and selecting a pressure-based steady-state solver, turbulence is simulated using the Reliable $k-\varepsilon$ model. The inlet boundary condition is defined as a velocity inlet with speeds of 10 m/s, 20 m/s, and 30 m/s. The outlet boundary condition is set as a pressure outlet. The pressure-velocity coupling algorithm is configured as COUPLED, employing a second-order upwind scheme for both momentum and turbulent energy discretization. The relaxation factor remains at its default value Mu et al. [32].

This methodology is employed to analyze the aerodynamic performance of the aircraft in flight. By varying the angle of attack, crucial aerodynamic parameters—such as lift coefficient, drag coefficient, and pitching moment coefficient—are derived and presented in Figure 11. From Figure 11, it is evident that variations in these aerodynamic parameters across different flight speeds can be effectively expressed through the angle of attack. The lift coefficient shows a direct correlation with both the angle of attack and speed, while the drag coefficient exhibits a linear relationship with the angle of attack, affirming that increased speed correlates with reduced drag.

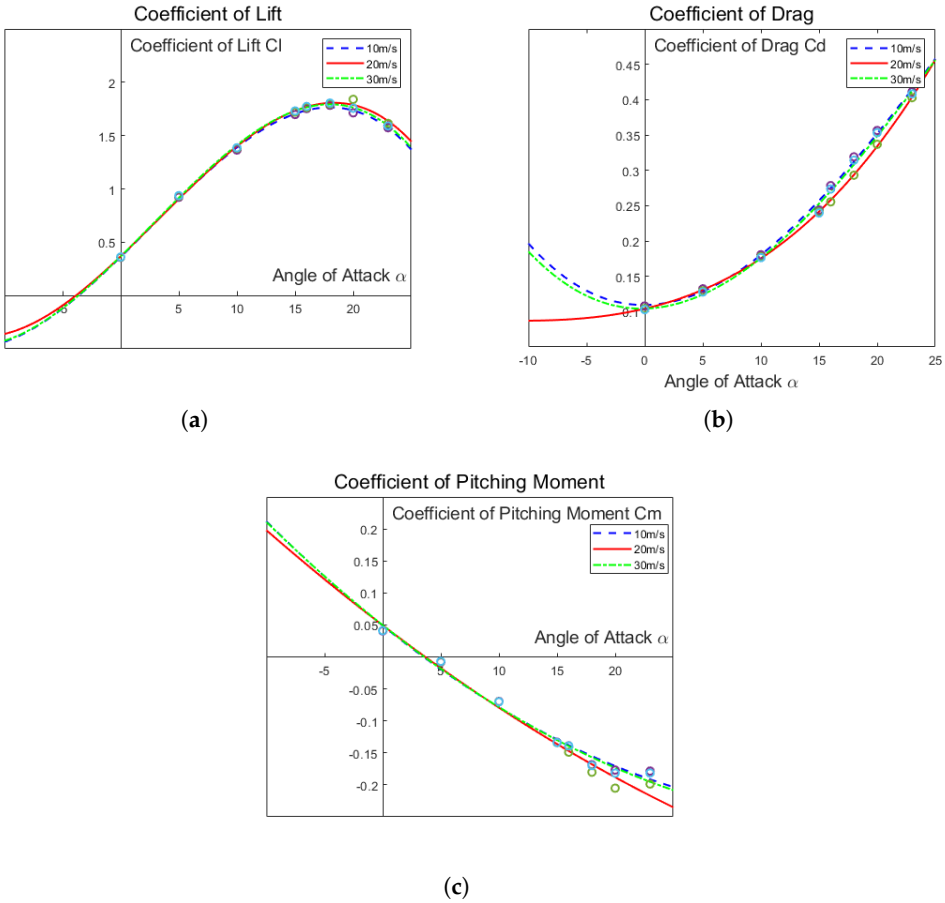

Figure 11. The aerodynamic parameters versus angle of attack. (**a**) Coefficient of lift varies with angle of attack; (**b**) Coefficient of drag varies with angle of attack; (**c**) Coefficient of pitching moment varies with angle.

Figure 12 illustrates the pressure distribution of the vehicle during aerial flight. As shown, the pressure peaks exhibit minor variations, primarily concentrated at the front of the fuselage, the leading edges of both the front and rear wings, and the leading edge of the X-type rudder. The streamlined fuselage shape results in minimal pressure discrepancies between the front and rear sections, leading to slight pressure differentials.

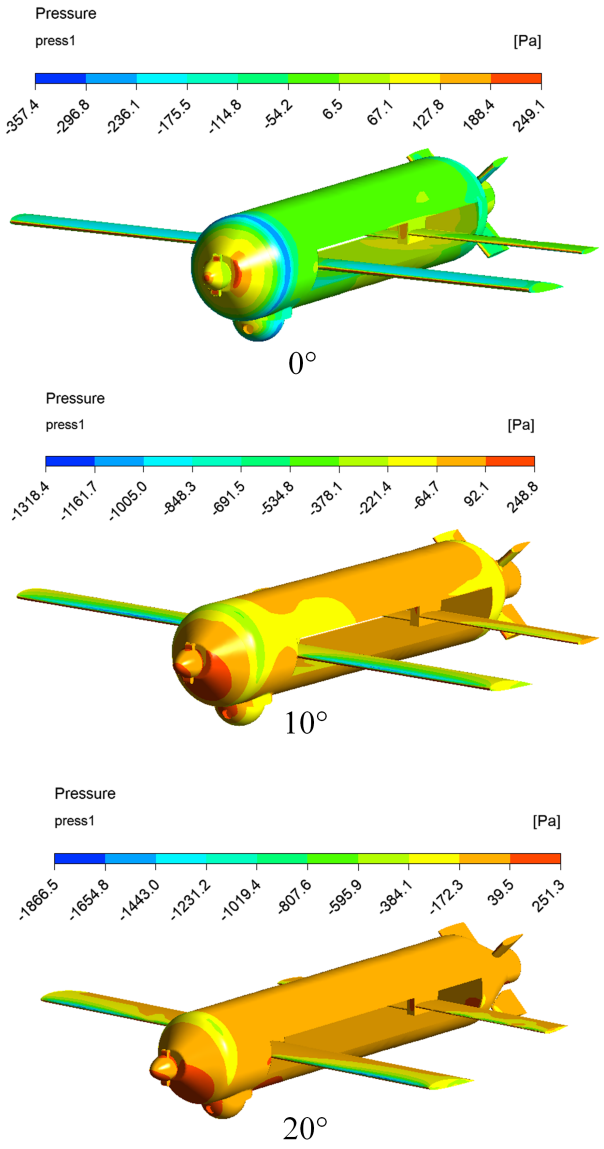

Figure 12. The pressure cloud of the vehicle in aerial flight state.

Figure 13 depicts the velocity distribution around the front and rear wing segments at the YZ plane along the midpoint of the aircraft. A notable high-velocity zone appears at the junction between the front fuselage and the upper central fuselage. Due to the fuselage's streamlined curvature, the transition of velocity in this region is gradual, preventing airflow separation. Conversely, airflow separation occurs at the rear segment of the fuselage, resulting in a low-speed region near the tail.

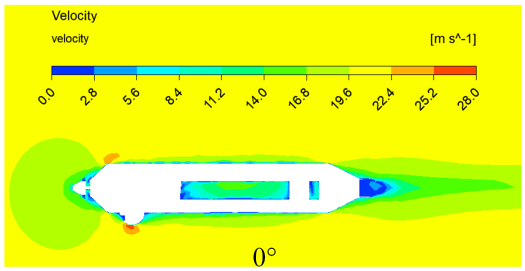

Figure 13. *Cont.*

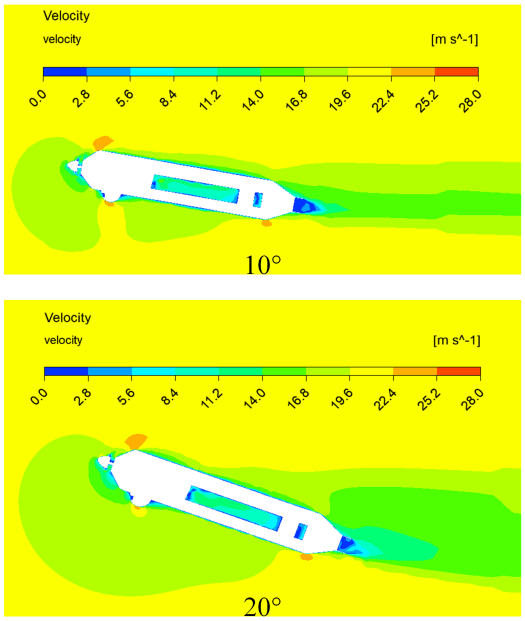

Figure 13. Velocity cloud of the front and rear wings sections of the vehicle in aerial flight state.

3.2. Underwater Fluid Simulation and Analysis

Using the aforementioned approach, we conduct aerodynamic assessments of the vehicle in an underwater environment. Figure 14 illustrates a simplified schematic of the underwater vehicle model.

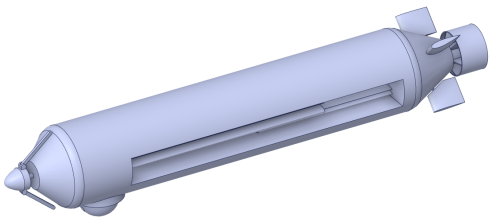

Figure 14. Simplified 3D model of the underwater submerged state.

Transitioning the fluid medium from air to liquid water, we establish inlet velocities of 2 m/s, 3 m/s, and 4 m/s. The vehicle's angle of attack is systematically varied from 0° to 30°, in increments of 5°.

Figure 15 presents the variations in three key hydrodynamic parameters—lift coefficient (Cl), drag coefficient (Cd), and pitching moment coefficient (Cm)—for the underwater vehicle across different velocities and angles of attack, ranging from −10° to 30°. The hydrodynamic parameters show minimal fluctuations within the velocity range of 2 m/s to 4 m/s, indicating consistency with the aerodynamic behavior observed in the air. Notably, unlike in air, the vehicle does not experience stalling phenomena underwater.

From the pressure distribution in Figure 16, a significant area of elevated pressure is observed beneath the front section of the fuselage. Negative pressure zones are primarily concentrated in the transition region between the front and central fuselage, characterized by substantial negative values. In contrast, the pressure in the fuselage's center remains relatively stable, gradually increasing towards the rear. With rising angles of attack, minimal changes occur in the maximum pressure and positive pressure zones along the fuselage. The negative pressure region exhibits limited variation, while the minimum pressure gradually decreases across the studied range.

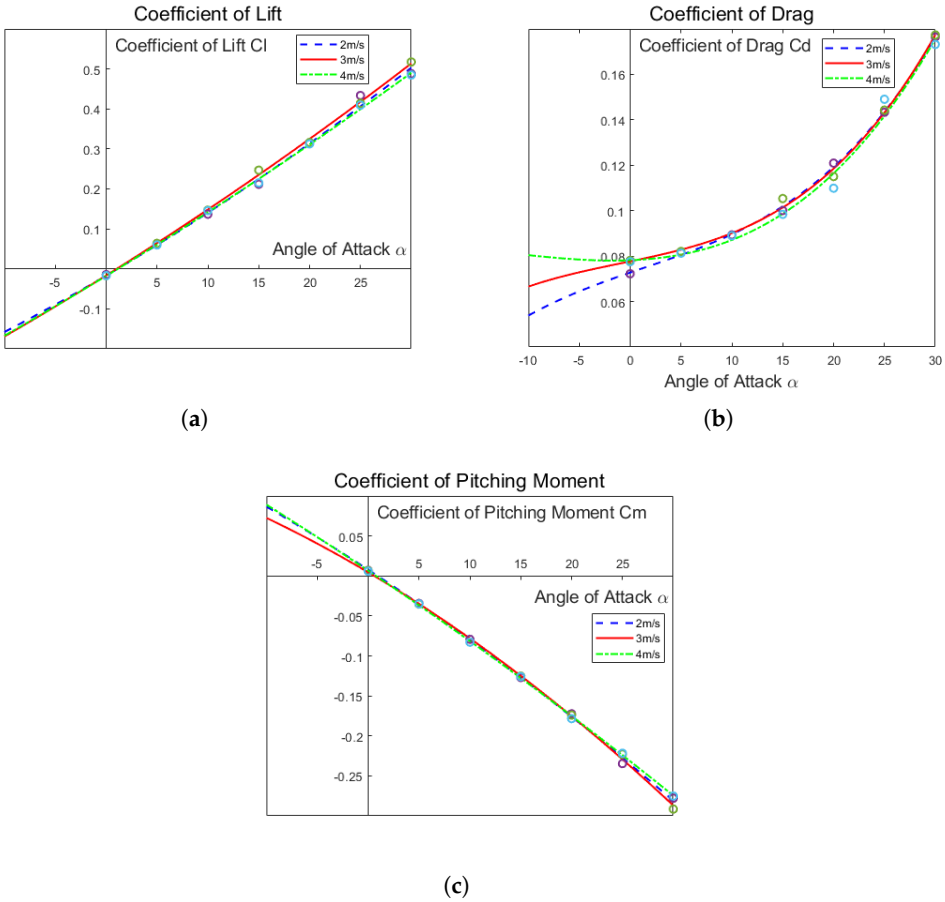

Figure 15. The hydrodynamic parameters versus angle of attack. (**a**) Coefficient of lift varies with angle of attack; (**b**) Coefficient of drag varies with angle of attack; (**c**) Coefficient of pitching moment varies with angle of attack.

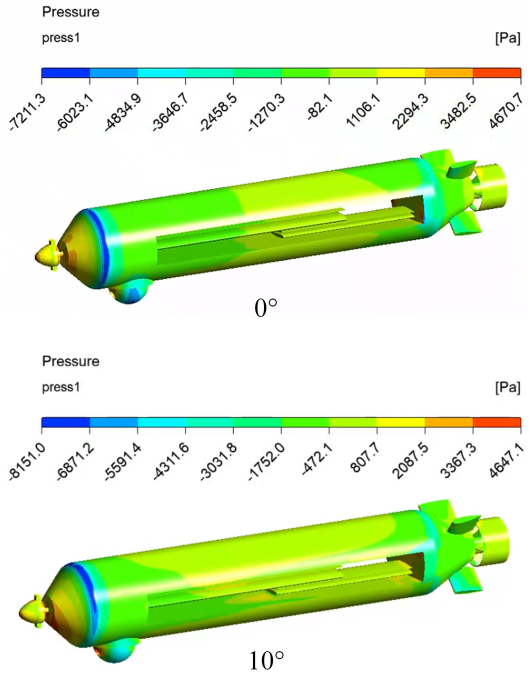

Figure 16. *Cont.*

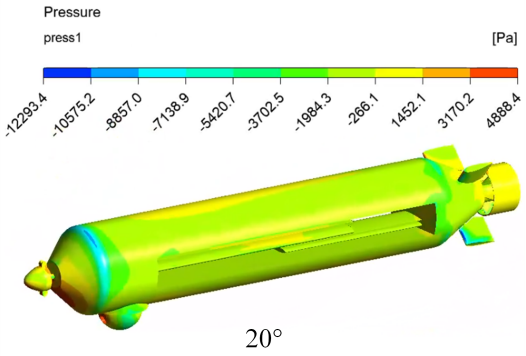

Figure 16. The pressure cloud of the vehicle in underwater submerged state.

Figure 17 shows the velocity distribution across the front and rear wing sections at the YZ plane along the vehicle's midpoint. High-speed zones are primarily concentrated in the upper segment of the fuselage at the front-to-center transition, around the propeller, and at the center-to-rear transition of the fuselage. The central fuselage experiences minimal speed fluctuations. A thin vorticity layer, induced by the viscous effects of water, adheres to the surface of the central fuselage due to frictional drag. Flow separation is noted at both the front and rear sections, leading to a low-pressure region at the rear.

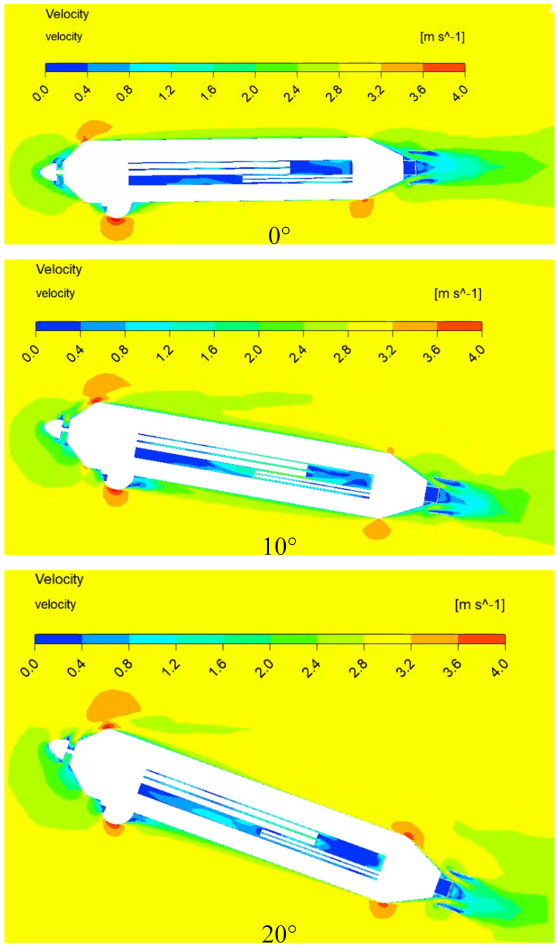

Figure 17. Velocity cloud of the front and rear wings sections of the vehicle in underwater submerged state.

3.3. The Air-to-Water Fluid Simulation

For the transmedia vehicle's water entry/exit scenario, an overlapping grid technique is employed. This method utilizes two mesh sets: a background mesh for the flow field and an object mesh encompassing the vehicle model to account for six degrees of freedom motion [33].

Following mesh generation, we define boundary conditions. Gravity acceleration is activated, and the pressure-based transient solver is selected. The simulation employs a two-phase flow Volume of Fluid (VOF) model for air and water, integrating the overlapping grid intersection. The start grid option is activated, and the vehicle's six degrees of freedom are configured, with the vehicle mass set at 1.5 kg and the inertia tensor specified.

Initial velocities of 20 m/s and 30 m/s are established for the vehicle. The angle between the vehicle and the water surface varies from 40° to 90°, with simulations conducted at 10° intervals. The process captures the vehicle's entry into the water, as depicted in Figure 18.

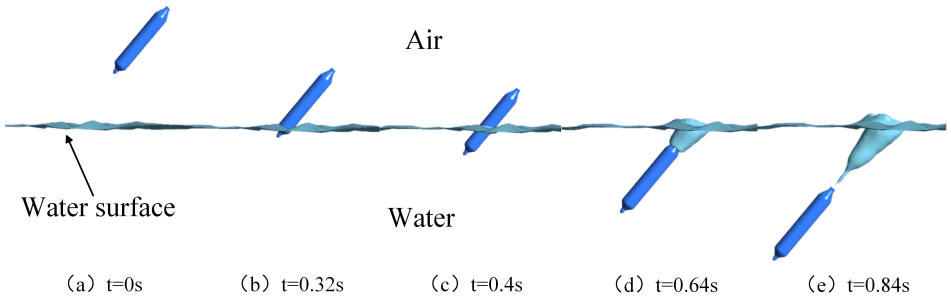

Figure 18. Air-to-water fluid simulation results.

A series of underwater numerical simulations were conducted to analyze the impact pressure on the front section of the vehicle's fuselage during various stages of the water entry process, as shown in Figure 19.

As seen in Figure 19, the impact force experienced during the underwater mode remains minimal until the vehicle contacts the water surface during the entry phase. Over time, as the vehicle descends further, the front portion of the fuselage contacts the water surface. Due to the significantly lower air density compared to water, the impact force rapidly escalates, reaching a peak value within a brief timeframe. Notably, the duration of this peak force is short-lived. Comparing maximum pressure peaks at different angles reveals that the vehicle experiences the smallest maximum impact force during water entry within the 40°–50° angle range.

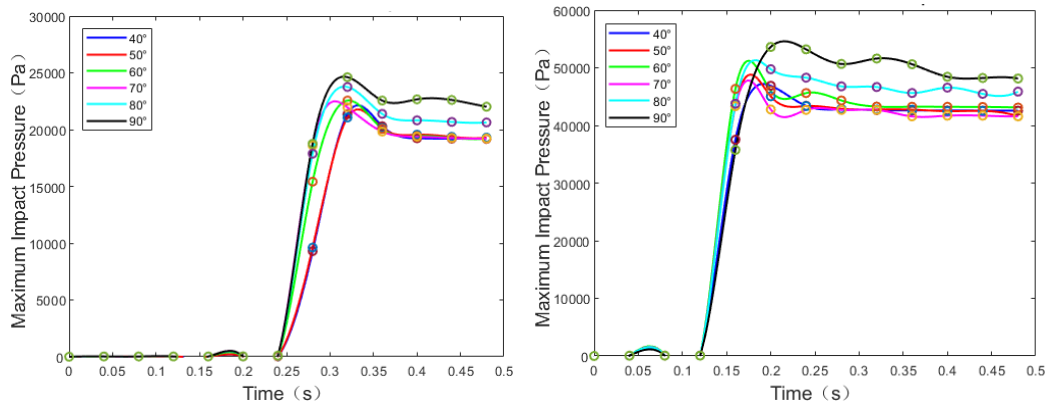

Figure 19. The impact of air-to-water at different velocity. (**a**) The impact of air-to-water at 20 m/s; (**b**) The impact of air-to-water at 30 m/s.

3.4. The Water-to-Air Fluid Simulation

For the vehicle's out-of-water scenario, the same two sets of grids—the flow field background grid and the object grid—are utilized, with adjustments made only to the encrypted section within the vehicle's operational region. The fluid computational domain of the outer flow field remains identical to that of the water entry computational domain.

The vehicle out-of-water problem adheres to the same boundary conditions as during water entry. Initial speeds of 3 m/s and 4 m/s are assigned to the vehicle, with the angle between the vehicle and the water surface varying from 40° to 90°, and simulations conducted at 10° intervals. A series of numerical simulations replicates the airborne modes of the aerial underwater vehicle as it exits the water.

Figure 20 illustrates the entire process of the vehicle exiting the water at a velocity of 3 m/s and an initial angle of 50° at different time intervals. At t = 0.24 s, the vehicle's nose gradually contacts and breaches the water surface. The water surface deforms, and a film adheres to the vehicle's surface due to viscosity effects. As the vehicle rises, the front wing emerges from the water, causing increased surface distortion. The water film clinging to the vehicle progressively dislodges from the nose towards the middle of the fuselage, expanding its coverage area.

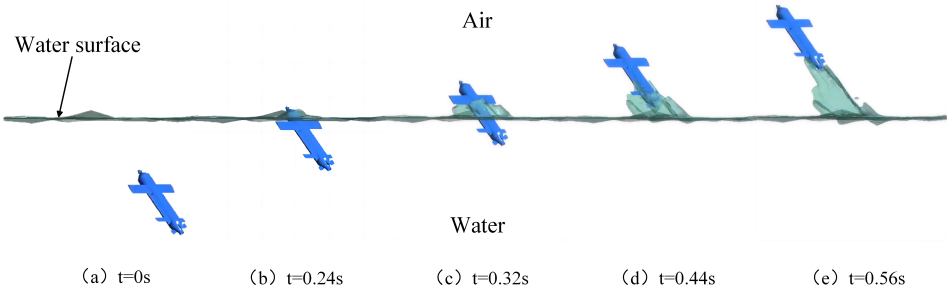

Figure 20. Water-to-air fluid simulation results.

The drag force and pitching moment of the vehicle during water exit are illustrated in Figure 21. It is evident from the figure that both the drag force and pitching moment show limited sensitivity to changes in the water exit angle but are significantly affected by the vehicle's speed. At a velocity of 3 m/s, the maximum drag force is approximately 75 N, and the maximum pitching moment is around 38 N·m. As the speed increases to 4 m/s, both the maximum drag force and pitching moment rise substantially, reaching about 130 N and 70 N·m, respectively. Notably, the curves of drag force and pitching moment versus time exhibit consistency across different speeds.

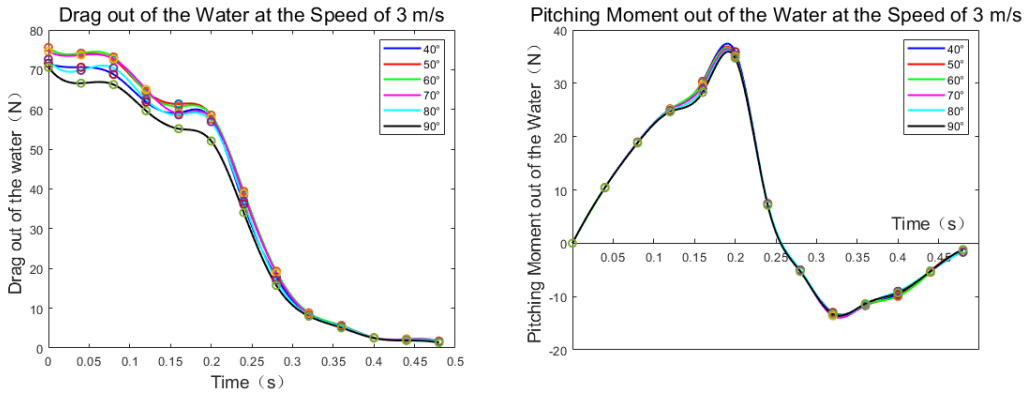

(**a**) (**b**)

Figure 21. *Cont.*

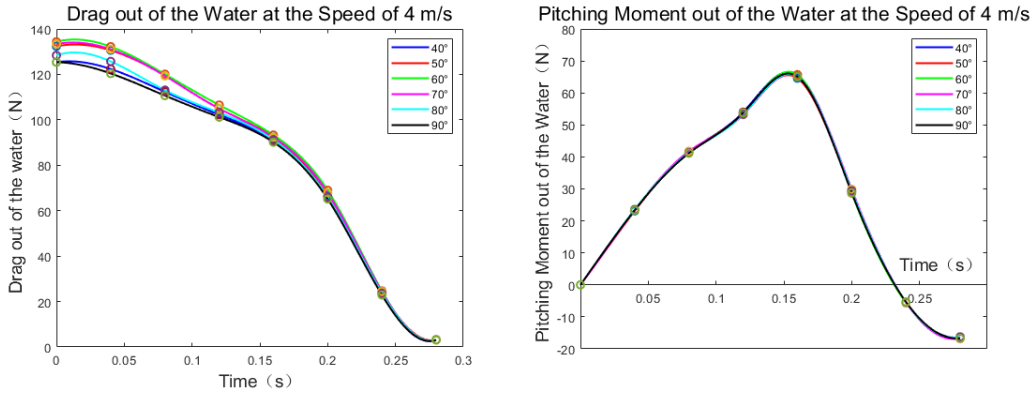

(**c**) (**d**)

Figure 21. Drag force and pitching moment at different speeds in near water surface state. (**a**) Coefficient of drag curve at 3 m/s; (**b**) Coefficient of pitching moment curveat 3 m/s; (**c**) Coefficient of drag curve at 4 m/s; (**d**) Coefficient of pitching moment curveat 4 m/s.

When comparing the vehicle's behavior in air and water, it is clear that the drag force and pitching moment experienced in air are considerably lower than those in water. Additionally, the pitching moment first decreases before rising to peak levels.

3.5. The Near Water Surface Fluid Simulation

For the near-surface scenario, the same grid setup used in the inlet simulation is applied, comprising both the flow field background grid and the object grid. The external flow field fluid computational domain mirrors the inlet computational domain, with grid refinement tailored for the near-surface region. The vehicle's near-surface object computational domain aligns with the inlet object computational domain.

During the vehicle's near-surface gliding phase, the boundary condition settings remain consistent with those used during water entry. Initial velocities of 10 m/s, 20 m/s, and 30 m/s are assigned to the vehicle, with the angle between the vehicle and the water surface set at −15°. Various modes of aerial underwater vehicle operation in different near-surface gliding states are obtained using these initial velocities.

Figure 22 illustrates the displacements of the center of mass at different velocity during the vehicle's near-surface gliding. Given the relatively minor velocities and accelerations in the yaw direction compared to the horizontal and vertical directions, yaw direction velocity and acceleration are not considered.

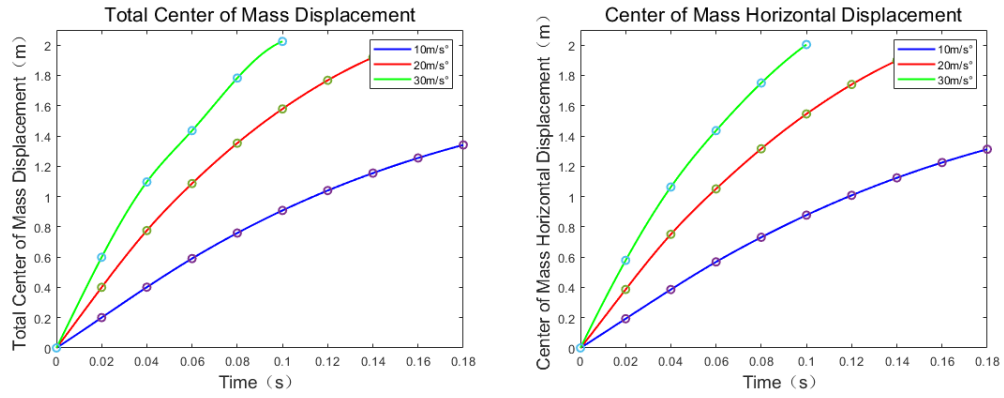

(**a**) (**b**)

Figure 22. *Cont.*

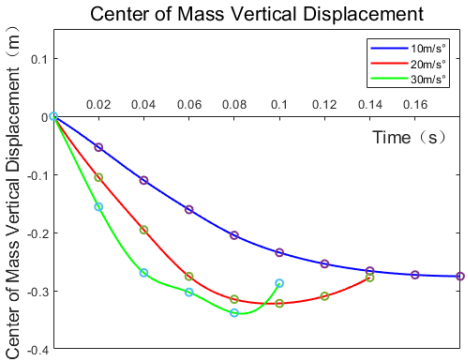

(**c**)

Figure 22. The center of mass displacement at different velocities in near water surface state. (**a**) The total displacement diagram of center of mass; (**b**) The horizontal displacement diagram of center of mass; (**c**) The vertical displacement diagram of center of mass.

From Figure 22, it is clear that the total displacement of the center of mass during the vehicle's near-surface water entry is predominantly influenced by horizontal displacement, with its trend closely mirroring that of the horizontal direction.

Prior to t = 0.06 s, the total center of mass displacement exhibits a linear increase, indicating that the vehicle is not fully submerged during this period. After t = 0.06 s, as the vehicle becomes completely submerged, the center of mass displacement follows a parabolic growth trajectory, with the growth rate gradually diminishing.

In terms of vertical displacement, the vehicle's center of mass initially experiences a linear decrease before t = 0.06 s, transitioning into a gradual parabolic descent after this point until reaching its lowest point. At this stage, the vehicle aligns parallel to the water surface due to buoyancy. Eventually, buoyancy causes the vehicle to raise its front, initiating an upward movement characterized by an increase in the vertical displacement of the center of mass.

Figure 23 presents the horizontal, vertical, and total displacements of the center of mass during the vehicle's near-surface water entry at different glide angles. The data indicate that gliding time increases when the angle between the vehicle and the water surface is zero compared to when it has a negative angle. Despite this difference in gliding time, the trends in center of mass displacement across all directions remain consistent. Notably, when the angle exceeds -10°, the vehicle can successfully re-leap out of the water after initial contact. As the angle increases, the time required for this re-leap decreases. Conversely, if the angle falls below −10°, the vehicle loses the ability to re-leap from the water surface.

Figure 24 depicts the entire process of the vehicle gliding near the surface of the water with an initial velocity of 20 m/s and an initial angle of 15° at different times. The vehicle is initially located near the water's surface. At t = 0.02 s, the front part of the vehicle fuselage begins to contact the water surface, and the vehicle is gradually submerged. As time progresses, after t = 0.04 s, the front part of the vehicle fuselage breaks through the water surface, creating a cavity at the rear. Due to the high speed, a cavity bubble forms at the front of the vehicle fuselage. Buoyancy influences the vehicle's pitch angle, causing the angle between the vehicle and the water surface to decrease while expanding the cavity range.

At t = 0.08 s, the air cavity at the rear of the vehicle reaches its maximum and gradually detaches from the fuselage surface. The vehicle becomes horizontal under the influence of buoyancy and begins to deflect upward. At this point, the vertical velocity of the vehicle changes from negative to positive, indicating upward movement. Due to water fluctuations, the vehicle experiences slight yaw in the horizontal direction.

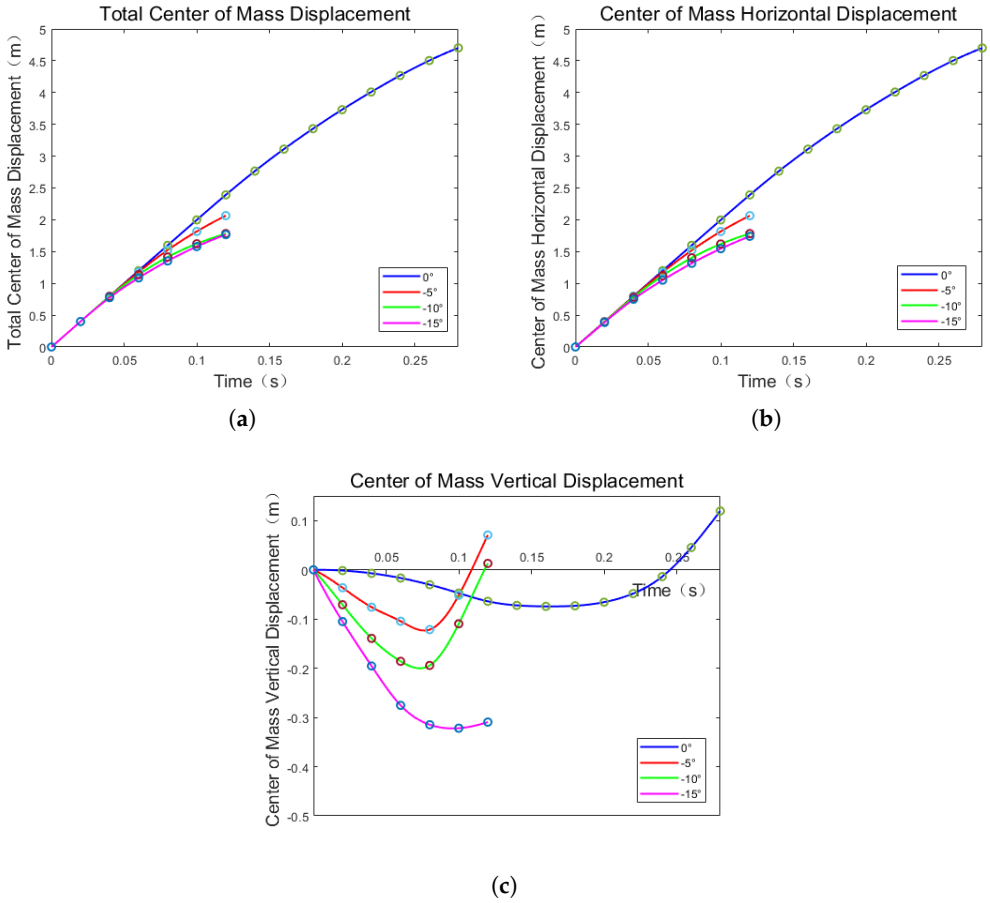

Figure 23. Vehicle center of mass displacement at different angles in near water surface state. (**a**) The total displacement diagram of center of mass; (**b**) The horizontal displacement diagram of center of mass; (**c**) The vertical displacement diagram of center of mass.

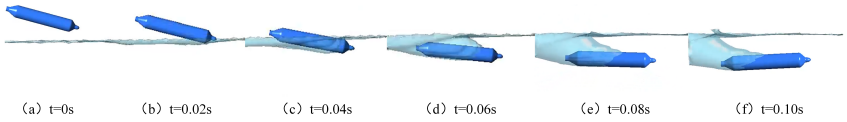

Figure 24. The near water surface fluid simulation results at the attack angle −15° and velocity 20 m/s.

The description outlines the boundary conditions and setup for the vehicle's near-water surface gliding state, indicating variations in gliding angle and initial velocity. The process involves the vehicle operating in underwater mode with different gliding angles. Figure 25 shows the near-water surface gliding process of the vehicle at different time points, considering an initial velocity of 20 m/s and varying initial gliding angles.

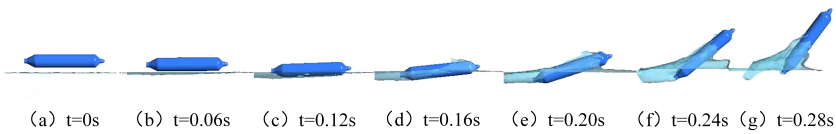

Figure 25. The near water surface fluid simulation results at the attack angle 0° and velocity 20 m/s.

4. Prototype and Experiments

Based on the theoretical research presented, we constructed a prototype of the hybrid aerial underwater vehicle. Initially, designing the hardware and software platform was

essential. We specified model requirements for various components, including batteries, motors, propellers, electric actuators, remote controls, map transmission modules, and GPS units, while carefully selecting materials for the wings and structural elements. The wings and frames are 3D printed by PLA materials. Subsequently, we completed the comprehensive installation of the hybrid aerial underwater vehicle prototype, as shown in Figure 26.

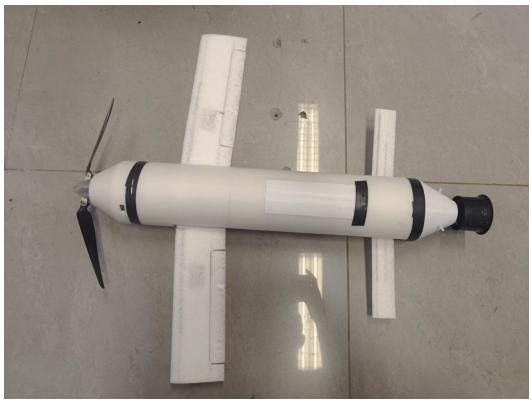

(**a**)

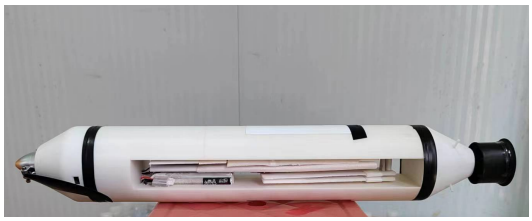

(**b**)

Figure 26. Prototype of the foldable hybrid aerial underwater vehicle. (**a**) Prototype of the foldable hybrid aerial underwater vehicle in deployed state; (**b**) Prototype of the foldable hybrid aerial underwater vehicle in folded state.

After calibrating each motor and the flight control system of the prototype, we advanced the electric actuators to extend both the front and rear wings. We then began assessing the prototype's flight feasibility, initiating the verification process. The flight sequence of the prototype is illustrated in Figure 27. The air cruising speed is about 61 km/h, which falls in the cruise speed range [10, 30] m/s analyzed in the simulation, as shown in Figure 11.

Figure 27. *Cont.*

Figure 27. The feasibility validation of aerial flight.

Finally, we applied waterproof sealing to protect all critical components of the prototype, including the battery, ESC, motor, flight control board, receiver, and the entire system. We retracted the actuator to fold the front and rear wings, allowing them to integrate seamlessly into the vehicle's body. The operational dynamics of the vehicle prototype on the water surface are visually depicted in Figure 28. The underwater speed is about 11 km/h, which falls in the underwater speed range [2, 4] m/s analyzed in the simulation, as shown in Figure 15. The experimental findings confirm the feasibility and effectiveness of the proposed prototype.

Figure 28. The feasibility validation of underwater submerging.

5. Conclusions

In this paper, we introduced a novel foldable hybrid aerial and underwater vehicle (HAUV) with an optimized design that enhances both aerodynamic and hydrodynamic performance. Through extensive computational fluid dynamics (CFD) simulations, we demonstrated the vehicle's capability to maintain stability during transitions between air and water environments, while also providing significant improvements in energy efficiency and thrust-to-weight ratio.

Key findings from the analysis show that:

- The foldable wing mechanism provides a marked improvement in both air and water maneuverability, reducing drag and optimizing lift generation during flight.
- The HAUV maintains a stable trajectory during aerial-to-underwater transitions, addressing a critical challenge in hybrid vehicle design.
- Hydrodynamic testing revealed that the vehicle achieves higher underwater speeds and reduced power consumption due to its streamlined structure and efficient propulsion system.
- Performance evaluation across different operational scenarios confirmed that the vehicle meets the demands of multi-environment missions, with specific benefits for marine exploration and search-and-rescue operations.

The results indicate that this design addresses key limitations in existing HAUVs, providing a more adaptable and efficient solution for complex missions that require both aerial and underwater capabilities. Future work will involve experimental validation of the prototype in real-world environments, as well as further refinement of the control algorithms to optimize the transition between mediums.

Author Contributions: Conceptualization, G.C. and L.Y.; methodology, G.C. and L.Y.; software, G.C., L.Y., A.C., X.Z., H.D. and Y.L.; validation, G.C., L.Y., A.C., X.Z., H.D. and Y.L.; formal analysis, G.C., L.Y., A.C., X.Z., H.D. and Y.L.; investigation, G.C. and L.Y.; resources, G.C.; data curation, G.C., L.Y., A.C., X.Z., H.D. and Y.L.; writing—original draft preparation, G.C. and L.Y.; writing—review and editing, G.C. and L.Y.; visualization, G.C., L.Y., A.C., X.Z., H.D. and Y.L.; supervision, G.C.; project administration, G.C.; funding acquisition, G.C. All authors have read and agreed to the published version of the manuscript.

Funding: This work was supported by National Key Research and Development Program of China (2022YFB4701600), National Natural Science Foundation of China (62103036), Beijing Natural Science Foundation (L243013), Central Government Guides Local Science and Technology Development Fund Projects (246Z1813G), and Fundamental Research Funds for the Central Universities (2024XKRC069).

Data Availability Statement: The original contributions presented in the study are included in the article, further inquiries can be directed to the corresponding author.

Conflicts of Interest: The authors declare no conflict of interest.

References

1. Yang, X.; Wang, T.; Liang, J.; Yao, G.; Liu, M. Survey on the novel hybrid aquatic–aerial amphibious aircraft: Aquatic unmanned aerial vehicle (AquaUAV). *Prog. Aerosp. Sci.* **2015**, *74*, 131–151. [CrossRef]
2. Suming, Q.; Weicheng, C. An overview on aquatic unmanned aerial vehicles. *Ann. Rev. Resear* **2019**, *5*, 555663.
3. Sun, Y.; Liu, X.; Cao, K.; Shen, H.; Li, Q.; Chen, G.; Xu, J.; Ji, A. Design and Theoretical Research on Aerial-Aquatic Vehicles: A Review. *J. Bionic Eng.* **2023**, *20*, 2512–2541. [CrossRef]
4. Hou, T.; Jin, D.; Gong, Y.; Wang, X.; Pei, X.; Yang, X. Frontier technology analysis and future prospects of aquatic un-manned aerial vehicle. *Sci. Technol. Rev.* **2023**, *41*, 5–22.
5. Zeng, Z.; Lyu, C.; Bi, Y.; Jin, Y.; Lu, D.; Lian, L. Review of hybrid aerial underwater vehicle: Cross-domain mobility and transitions control. *Ocean Eng.* **2022**, *248*, 110840. [CrossRef]
6. Yao, G.; Li, Y.; Zhang, H.; Jiang, Y.; Wang, T.; Sun, F.; Yang, X. Review of hybrid aquatic-aerial vehicle (HAAV): Classifications, current status, applications, challenges and technology perspectives. *Prog. Aerosp. Sci.* **2023**, *139*, 100902. [CrossRef]
7. Sun, X.; Cao, J.; Li, Y.; Wang, B. Design and field test of a foldable wing unmanned aerial–underwater vehicle. *J. Field Robot.* **2024**, *41*, 347–373. [CrossRef]
8. Jin, Y.; Bi, Y.; Lyu, C.; Bai, Y.; Zeng, Z.; Lian, L. Nezha-IV: A hybrid aerial underwater vehicle in real ocean environments. *J. Field Robot.* **2024**, *41*, 420–442. [CrossRef]
9. Bi, Y.; Lu, D.; Zeng, Z.; Lian, L. Dynamics and control of hybrid aerial underwater vehicle subject to disturbances. *Ocean Eng.* **2022**, *250*, 110933. [CrossRef]
10. Lu, D.; Xiong, C.; Zhou, H.; Lyu, C.; Hu, R.; Yu, C.; Zeng, Z.; Lian, L. Design, fabrication, and characterization of a multimodal hybrid aerial underwater vehicle. *Ocean Eng.* **2021**, *219*, 108324. [CrossRef]
11. Lyu, C.; Lu, D.; Xiong, C.; Hu, R.; Jin, Y.; Wang, J.; Zeng, Z.; Lian, L. Toward a gliding hybrid aerial underwater vehicle: Design, fabrication, and experiments. *J. Field Robot.* **2022**, *39*, 543–556. [CrossRef]
12. Lu, D.; Xiong, C.; Zeng, Z.; Lian, L. Adaptive dynamic surface control for a hybrid aerial underwater vehicle with parametric dynamics and uncertainties. *IEEE J. Ocean Eng.* **2019**, *45*, 740–758. [CrossRef]
13. Aoki, V.M.; Pinheiro, P.M.; Drews, P.L., Jr.; Cunha, M.A.; Tuchtenhagen, L.G. Analysis of a hybrid unmanned aerial underwater vehicle considering the environment transition. In Proceedings of the 2021 Latin American Robotics Symposium (LARS), 2021 Brazilian Symposium on Robotics (SBR), and 2021 Workshop on Robotics in Education (WRE), Natal, Brazil, 11–15 October 2021; pp. 90–95.
14. Ravell, D.A.M.; Maia, M.M.; Diez, F.J. Modeling and control of unmanned aerial/underwater vehicles using hybrid control. *Control Eng. Pract.* **2018**, *76*, 112–122. [CrossRef]
15. Horn, A.C.; Pinheiro, P.M.; Grando, R.B.; Da Silva, C.B.; Neto, A.A.; Drews, P.L. A novel concept for hybrid unmanned aerial underwater vehicles focused on aquatic performance. In Proceedings of the 2020 Latin American Robotics Symposium (LARS), 2020 Brazilian Symposium on Robotics (SBR) and 2020 Workshop on Robotics in Education (WRE), Natal, Brazil, 9–13 November 2020; pp. 1–6.
16. Grando, R.B.; de Jesus, J.C.; Kich, V.A.; Kolling, A.H.; Bortoluzzi, N.P.; Pinheiro, P.M.; Neto, A.A.; Drews, P.L. Deep reinforcement learning for mapless navigation of a hybrid aerial underwater vehicle with medium transition. In Proceedings of the 2021 IEEE International Conference on Robotics and Automation (ICRA), Xi'an, China, 30 May–5 June 2021; pp. 1088–1094.
17. Ba, K.; Chen, C.; Ma, G.; Song, Y.; Wang, Y.; Yu, B.; Kong, X. A compensation strategy of end-effector pose precision based on the virtual constraints for serial robots with RDOFs. *Fundam. Res.* 2024, *in press*. [CrossRef]
18. Zimmerman, S.; Abdelkefi, A. Review of marine animals and bioinspired robotic vehicles: Classifications and characteristics. *Prog. Aerosp. Sci.* **2017**, *93*, 95–119. [CrossRef]

19. Zimmerman, S.; Abdelkefi, A. Investigations on the buckling and dynamics of diving-inspired systems when entering water. *Bioinspiration Biomimetics* **2020**, *15*, 036015. [CrossRef]
20. Zimmerman, S. Nonlinear Dynamics and Buckling Characteristics of Gannet-Inspired Systems During Diving. Ph.D. Thesis, New Mexico State University, Las Cruces, NM, USA, 2020.
21. Zimmerman, S.; Abdelkefi, A. Considerations for increasing the survivability of Gannet-inspired drones during diving. *Ocean Eng.* **2021**, *238*, 109681. [CrossRef]
22. Pena, I.; Billingsley, E.; Zimmerman, S.; Vasconcellos, R.; Abdelkefi, A. Comprehensive sizing process, actuation mechanism selection, and development of gannet-inspired amphibious drones. In Proceedings of the AIAA AVIATION 2020 FORUM, Online, 15–19 June 2020; p. 2764.
23. Pena, I. Performance Analysis and Design Process of Gannet-inspired Aerial-aquatic Drones. Master's Thesis, New Mexico State University, Las Cruces, NM, USA, 2020.
24. Wang, X.; Yang, X.; Zhao, J.; Pei, X.; Su, H.; Wang, T.; Hou, T. Aquatic unmanned aerial vehicles (AquaUAV): Bionic prototypes, key technologies, analysis methods, and potential solutions. *Sci. China Technol. Sci.* **2023**, *66*, 2308–2331. [CrossRef]
25. Wang, X.; Pei, X.; Wu, J.; Wang, X.; Hou, T. Design, fabrication and fine-tuning of an aerial-aquatic explosive water-jet thruster with repeatable propulsion capability. In Proceedings of the 2023 IEEE International Conference on Robotics and Biomimetics (ROBIO), Koh Samui, Thailand, 4–9 December 2023; pp. 1–6.
26. Gan, W.; Zuo, Z.; Zhuang, J.; Bie, D.; Xiang, J. Aerodynamic/Hydrodynamic Investigation of Water Cross-Over for a Bionic Unmanned Aquatic–Aerial Amphibious Vehicle. *Biomimetics* **2024**, *9*, 181. [CrossRef]
27. Yan, L.; Cao, A.; Zhu, X.; Ding, H.; Lu, H.; Chen, G. Design and Analysis of a Novel Hybrid Aerial Underwater Vehicle with Foldable Wings. In Proceedings of the 2024 36th Chinese Control and Decision Conference (CCDC), Xi'an, China, 25–27 May 2024; pp. 361–366.
28. Yan, L.; Cao, A.; Zhu, X.; Ding, H.; Lu, H.; Chen, G. Novel Design for a Hybrid Aerial Underwater Vehicle. In Proceedings of the 2024 10th International Conference on Electrical Engineering, Control and Robotics (EECR), Guangzhou, China, 29–31 March 2024; pp. 215–219.
29. Yan, L.; Cao, A.; Zhu, X.; Ding, H.; Guo, S.; Chen, G. Mechanical Design and Fluid Dynamics Simulation of a Reconfigurable Hybrid Aerial Underwater Vehicle. In Proceedings of the 2024 6th International Conference on Reconfigurable Mechanisms and Robots (ReMAR), Chicago, IL, USA, 23–26 June 2024; pp. 548–553.
30. Chen, T.; Huang, W.; Zhang, W.; Qi, Y.; Guo, Z. Experimental investigation on trajectory stability of high-speed water entry projectiles. *Ocean Eng.* **2019**, *175*, 16–24. [CrossRef]
31. Hou, T.; Yang, X.; Su, H.; Chen, L.; Wang, T.; Liang, J.; Zhang, S. Design, fabrication and morphing mechanism of soft fins and arms of a squid-like aquatic-aerial vehicle with morphology tradeoff. In Proceedings of the 2019 IEEE International Conference on Robotics and Biomimetics (ROBIO), Dali, China, 6–8 December 2019; pp. 1020–1026.
32. Mu, Q.; Xiong, T.; Wang, K.; Yi, W.; Jun, G. Numerical simulation for high speed oblique water entry of different density projectiles. In *Proceedings of the Journal of Physics: Conference Series*; IOP Publishing: Bristol, UK, 2020; Volume 1507, p. 102028.
33. Clain, S.; Lopes, D.; Pereira, R.M. Very high-order Cartesian-grid finite difference method on arbitrary geometries. *J. Comput. Phys.* **2021**, *434*, 110217. [CrossRef]